Fabry–Perot interferometer based Mie Doppler lidar for low tropospheric wind observation

Haiyun Xia,[1,*] Dongsong Sun,[2] Yuanhong Yang,[1] Fahua Shen,[2] Jingjing Dong,[2] and Takao Kobayashi[3]

[1]Institute of Opto-electronics Technology, Beihang University, Beijing 100083, China
[2]Anhui Institute of Optics and Fine Mechanics, Chinese Academy of Sciences, Hefei 230031, China
[3]University of Fukui, 3-9-1 Bunkyo, Fukui 910-8507, Japan

*Corresponding author: haiyunxia@126.com

Received 25 April 2007; revised 30 July 2007; accepted 8 August 2007;
posted 8 August 2007 (Doc. ID 82393); published 3 October 2007

Similar in principle to recent implementations of a lidar system at 355 nm [Opt. Lett. **25,** 1231 (2000), Appl. Opt. **44,** 6023 (2005)], an incoherent-detection Mie Doppler wind lidar at 1064 nm was developed and deployed in 2005 [Opt. Rev. **12,** 409 (2005)] for wind measurements in the low troposphere, taking advantage of aerosol scattering for signal enhancement. We present a number of improvements made to the original 1064 nm system to increase its robustness for long-period operation. These include a multimode fiber for receiving the reference signal, a mode scrambler to allow uniform illumination over the Fabry–Perot interferometer, and a fast scannable Fabry–Perot interferometer for calibration and for the determination of outgoing laser frequency during the wind observation. With these improvements in stability, the standard deviation of peak transmission and FWHM of the Fabry–Perot interferometer was determined to be 0.49% and 0.36%, respectively. The lidar wind measurements were validated within a dynamic range of ± 40 m/s. Comparison experiments with both wind profiler radar and Vaisala wiresonde show good agreement with expected observation error. An example of 24 h continuous observations of wind field and aerosol backscatter coefficients in the boundary layer with 1 min and 30 m temporal and spatial resolution and 3 m/s tolerated wind velocity error is presented and fully demonstrates the stability and robustness of this lidar.

OCIS codes: 010.0010, 010.3640, 280.0280, 280.3340, 280.1100.

1. Introduction

The wind profiles throughout the troposphere and lower stratosphere are critical for improving long-range weather forecasting, hurricane tracking, troposphere-stratosphere exchange studies, global pollution tracing, and climate studies. Such measurements are ranked as one of the most important and challenging observations to make [1]. The incoherent Doppler wind lidar (DWL) has been proved to be a promising technique that will fulfill the unmet information of the global wind fields with the needed accuracy and spatial resolution [2].

DWL instrument concepts can be divided into two main categories. One approach is optical heterodyning lidar, which measures Doppler shifts by beating the backscattered laser light with a laser source from a stable local oscillator [3,4]. The other is direct detection lidar (DDL). Various instruments, such as the Fabry–Perot interferometer (FPI) [5–10], iodine absorption filter [11,12], Fizeau interferometer [13], and Mach–Zehnder interferometer [14] have been chosen theoretically and experimentally to transform the Doppler shift into an irradiance variation, and the estimate of the frequency change can be accomplished by processing the detected signals. There are usually two leading implementations of the DDL when an FPI is used as the frequency discriminator. One is called the edge technique, which usually uses two FPI filters located at the wings of the atmospheric Rayleigh spectrum or two narrow filters with opposite slopes symmetrically located about the laser frequency to discriminate the Doppler shift from the

0003-6935/07/297120-12$15.00/0

Rayleigh or the Mie backscatter [5–8]. The other is the fringe-imaging technique. Several fringe-imaging DDL systems have been developed by Michigan Aerospace Corporation using a circular image plane detector or a circle-to-line imaging optic device [9,10]. The two implementations have been compared theoretically [15–17]. The DDL technique has been chosen by the European Space Agency as the basis of the AEOLUS space-based wind lidar mission [18].

The wind velocity measurement in the upper troposphere and stratosphere was realized mainly by detecting the molecular Rayleigh backscatter [19–22]. In the low troposphere, aerosols provide a near-ideal scattering source, because Mie backscattering is not significantly broadened from the original laser bandwidth [23–27]. Thus, the Mie Doppler lidar using the double-edge technique can achieve a higher sensitivity value of ten times the Rayleigh Doppler lidar [7,8]. The double-edge technique allows the Rayleigh and aerosol components of the atmospheric echo to be separated, on the assumption that accurate atmospheric temperature and pressure profiles were acquirable simultaneously to calculate the Rayleigh–Brillouin spectra [28]. Although eye safety is difficult to realize, we operate at 1064 nm instead of at 532 or 355 nm to take advantage of the lower molecular-to-aerosol backscatter ratio to ensure that the measurement is less sensitive to the spectral width and shape of the molecular signal.

Section 2 gives a review of the theory. Section 3 presents a description of the instrumental setup, followed by some improvements made to the original system. Section 4 presents the detailed calibration process and validation experiments. Comparison between theoretical analysis and measured errors are also performed. Section 5 gives comparison experiments with both wind profiler radar and Vaisala wiresonde. Examples of continuous observation of the wind field and aerosol backscatter coefficients are given.

2. Principle of Measurement

The edge technique is a direct detection method for retrieving the instantaneous wind information by making differential measurement of the Doppler-shifted atmospheric echo and the outgoing laser pulse. The double-edge technique is a variation of the edge technique. It inherits the advantages of edge technique but has a higher measurement accuracy and allows the Rayleigh and aerosol components of the atmospheric backscatter to be separated [7].

In this paper, a twin-channel FPI is used as the frequency discriminator to detect the Doppler shift. It consists of two channels with different cavity spacing that forms the transmission curves as shown in Fig. 1. The interferometer is illuminated by a fiber collimated on the two semicircles with an angular field of view of $\theta_{max} = 0.5$ mrad (semi-angle). Therefore, the edge function is the result of the integration of the Airy function over θ:

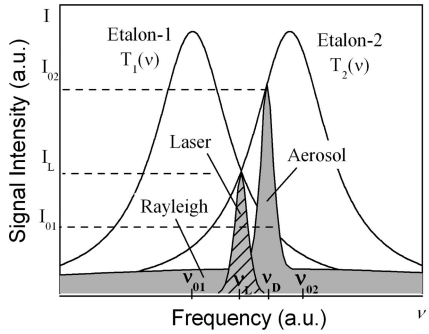

Fig. 1. Spectral profiles of the FPI, laser, and atmospheric backscatter signals.

$$h(\nu) = \int_0^{\theta_{max}} \frac{T_0}{1 + 4\left(\frac{\nu_{FSR}}{\pi\Delta\nu_{1/2}}\right)^2 \sin^2\left[\frac{\pi\nu\cos(\theta)}{\nu_{FSR}}\right]} \, d\theta. \quad (1)$$

In this expression, T_0 is the peak transmission, ν_{FSR} is the free-spectral range, and $\Delta\nu_{1/2}$ is the full width at half maximum (FWHM) of the interferometer. In the system, the frequency offset ($\Delta\nu_{21} = \nu_{02} - \nu_{01}$) of the twin-channel interferometer is designed to be 200 MHz, corresponding to a speed dynamic range of ± 50 m/s. The FWHM of the interferometer is $\sim$170 MHz. The outgoing laser frequency is locked at the crossing point of the two curves. The backscatter signal is Doppler shifted due to the atmosphere bulk movement projected in the line of sight (LOS) of the telescope. Its transmittance through the FPI varies with the magnitude of the Doppler shift. By making differential measurement of the transmittances of outgoing laser and the atmospheric backscatter signal, one can retrieve the spectral Doppler shift.

Radial wind, the bulk motion of air in sight of light, causes an overall spectral Doppler shift $\Delta\nu_d$, and the random thermal motions of the air particles spectrally broaden the backscattered signal. The aerosol and molecule backscatter spectra, $f_M(\nu)$ and $f_R(\nu)$, respectively, have Gaussian profile. They are given by

$$f_M(\nu) = \left(4\ln 2/\pi\Delta\nu_M^2\right)^{1/2} \exp\left(-\nu^2 4\ln 2/\Delta\nu_M^2\right), \quad (2)$$

$$f_R(\nu) = \left(4\ln 2/\pi\Delta\nu_R^2\right)^{1/2} \exp\left(-\nu^2 4\ln 2/\Delta\nu_R^2\right), \quad (3)$$

where $\Delta\nu_M$ is the FWHM of the aerosol backscatter spectrum. It can be replaced by the corresponding value of outgoing laser $\Delta\nu_L$ since the Brownian motion of aerosol particles does not broaden the spectrum significantly. Hence, the outgoing laser spectrum $f_L(\nu)$ can substitute for the aerosol backscatter spectrum $f_M(\nu)$ in this paper.

The FWHM of the atmospheric molecular spectrum $\Delta\nu_R$ is given by

$$\Delta\nu_R = \left(32kT_a \ln 2/\lambda^2 M\right)^{1/2}, \quad (4)$$

where k is the Boltzmann constant, T_a is the atmospheric temperature, M is the averaging mass of the

atmospheric molecules, and λ is the laser wavelength. The transmission of the ith ($i = 1, 2$) interferometer channel for Mie backscatter is written as a convolution function by

$$T_{Mi}(\nu) = \int_{-\infty}^{\infty} h_i(\nu - \nu') f_M(\nu') \mathrm{d}\nu' = \int_{-\infty}^{\infty} h_i(\nu - \nu') f_L(\nu') \mathrm{d}\nu', \quad (5)$$

where $h_i(\nu)$ is the ith edge function of the individual FPI channel. The FPI transmission functions for Rayleigh backscatter are a convolution of the edge function, laser spectrum, and the Rayleigh spectrum. They can be written as

$$T_{Ri}(\nu) = \int_{-\infty}^{\infty} T_{Mi}(\nu - \nu') f_R(\nu') \mathrm{d}\nu'. \quad (6)$$

The transmission functions $T_{Mi}(\nu)$ can be measured conveniently by scanning FPI cavity spacing using a pulsed laser. It is discussed in detail in Section 4. But in the low boundary layer, due to the altitude-dependent temperature and pressure effects, Eq. (6) is no longer a correct representation. In the data process, the Rayleigh–Brillouin spectra have to be used instead of Eq. (3) [28]. The transmitted signals measured on the different channels are

$$I_1 = a_1[I_M T_{M1}(\nu_0 + \Delta\nu_d) + I_R T_{R1}(\nu_0 + \Delta\nu_d)], \quad (7a)$$

$$I_2 = a_2[I_M T_{M2}(\nu_0 + \Delta\nu_d) + I_R T_{R2}(\nu_0 + \Delta\nu_d)], \quad (7b)$$

where a_1 and a_2 are calibration constants and both can be determined in the calibration process, as described in Section 4. $\Delta\nu_d$ is the Doppler shifted frequency, ν_0 is the outgoing laser frequency, and I_M and I_R are the aerosol signal and the Rayleigh signal, respectively. The energy monitoring channels are broad with respect to the Rayleigh backscatter, so the signals measured corresponding to the two channels are

$$I_{E1} = a_3(I_M + I_R), \quad (8a)$$

$$I_{E2} = a_4(I_M + I_R), \quad (8b)$$

where a_3 and a_4 are two calibration constants. In the case of reference signal incidence, it follows from Eqs. (7) and (8) that

$$T_{M1}(\nu_0) = \frac{a_3 I_1}{a_1 I_{E1}}, \quad (9a)$$

$$T_{M2}(\nu_0) = \frac{a_4 I_2}{a_2 I_{E2}}. \quad (9b)$$

One can solve Eq. (9) for the outgoing laser frequency ν_0 on both channels of the interferometer with the pre-probed transmission curves $T_{Mi}(\nu)$.

The lidar system is designed to analyze the Doppler shift from the Mie backscatter of the atmospheric aerosols, but the atmospheric echo collected is the superposition of aerosol and melocular components. The transmittance change due to the Doppler shift of Rayleigh backscatter is different from that of the Mie backscatter, so the Rayleigh components can be subtracted from the whole backscatter during the data processing. From Eq. (8) it follows that

$$I_E = (a_3 + a_4)(I_M + I_R). \quad (10)$$

The outgoing laser frequency ν_0 is measured in advance from Eq. (9). So nonlinear Eqs. (7) and (10) can be solved using the numerical iteration method for the Doppler shift $\Delta\nu_d$, aerosol signal I_M, and the Rayleigh signal I_R, respectively.

Iterative method is used to solve the nonlinear equations. In the iterative procedure, sufficiently accurate starting values guarantee the fast convergence. So, the Klett and Fernald methods are used to evaluate the starting values of I_M and I_R [29–31].

Step 1: It follows from Eq. (10) that

$$I_R = I_E/(a_3 + a_4) - I_M. \quad (11)$$

Step 2: From Eqs. (7) and (11), we can define

$$F_i(\Delta\nu_d, I_M) = I_M T_{Mi}(\nu_0 + \Delta\nu_d) + I_R T_{Ri}(\nu_0 + \Delta\nu_d) - I_i/a_i. \quad (12)$$

Then two computing corrections $\delta\nu_d$ and δI_M to the variables $\Delta\nu_d$ and I_M can be calculated by solving the following linear equations:

$$\begin{bmatrix} \delta\nu_d \\ \delta I_M \end{bmatrix} \begin{bmatrix} \dfrac{F_1(\Delta\nu_d + h, I_M) - F_1(\Delta\nu_d, I_M)}{h} & \dfrac{\partial F_1}{\partial I_M} \\ \dfrac{F_2(\Delta\nu_d + h, I_M) - F_2(\Delta\nu_d, I_M)}{h} & \dfrac{\partial F_2}{\partial I_M} \end{bmatrix} = -\begin{bmatrix} F_1(\Delta\nu_d, I_M) \\ F_2(\Delta\nu_d, I_M) \end{bmatrix}, \quad (13)$$

where $h = 100$ Hz, so the finite difference approximations inside the Jacobian matrix can substitute the partial derivatives $\partial F_i/\partial\Delta\nu_d$.

Step 3: Update the Doppler shift $\Delta\nu_d$ and aerosol signal I_M,

$$\Delta\nu_d^{(N)} = \Delta\nu_d^{(N-1)} + \delta\nu_d, \quad (14)$$

$$I_M^{(N)} = I_M^{(N-1)} + \delta I_M, \quad (15)$$

where N is the iterative index. This procedure is iterated until the variables $\Delta\nu_d$ and I_M converge or the iterative index exceeds the maximum number of it-

erations. The wind speed usually changes gently between the two adjacent intervals, so the Doppler shift value in the neighboring interval just beneath the interval being analyzed can be used as the initial value of $\Delta\nu_d$ in Eq. (12).

Once the Doppler shift is obtained, the LOS wind velocity can be retrieved:

$$V = \frac{c}{2\nu_0}\,\Delta\nu_d. \tag{16}$$

Three laser beams are pointed to every 120° azimuth sequentially with a 45° zenith angle; the first beam is pointed to the east. Data are accumulated every 200 ns according to 30 m range resolution. The radial wind velocities are observed clockwise, namely, V_1, V_2, and V_3. Then the wind velocity is

$$V_H = \frac{2\sqrt{2}}{3}\left(V_1^2 + V_2^2 + V_3^2 - V_1V_2 - V_2V_3 - V_1V_3\right)^{1/2}, \tag{17}$$

$$V_Z = \frac{\sqrt{2}}{3}(V_1 + V_2 + V_3), \tag{18}$$

$$\theta = -\arctan\left(\frac{\sqrt{3}(V_3 - V_2)}{2V_1 - V_2 - V_3}\right) - \frac{\pi}{2}\,\mathrm{sgn}\left(\frac{\sqrt{2}}{3}(2V_1 - V_2 - V_3)\right), \tag{19}$$

where V_H and V_Z are horizontal and vertical wind components, respectively. θ is the angle of the wind direction from the south in clockwise. Vertical winds are usually on the verge of zero, so observations of large, sustained vertical winds may indicate an instrument maladjustment.

3. System Description

DWL is an active remote sensing instrument that uses aerosol and/or molecular backscatter to measure wind. Specifically, the atmospheric backscatter from a laser pulse is collected by a telescope, range-gated, and spectrally analyzed to determine the Doppler shift. Figure 2 shows the schematic of the coaxial DWL system. The system parameters are summarized in Table 1. The transmitter is a 1064 nm injection-seeded Nd:YAG laser (Continuum Model 8050). The outgoing laser beam is directed through an 8× expander to compress the beam divergence. Before that, a very small fraction of the outgoing laser is split out by beam splitter (BS) 1 as a reference signal to determine its frequency. A 300 mm aperture scanner is mounted on the roof of the laboratory, providing full hemispherical pointing. The major portion of the laser energy is sent out and backscattered by the atmospheric aerosols and molecules. Atmospheric backscatter that carries Doppler information

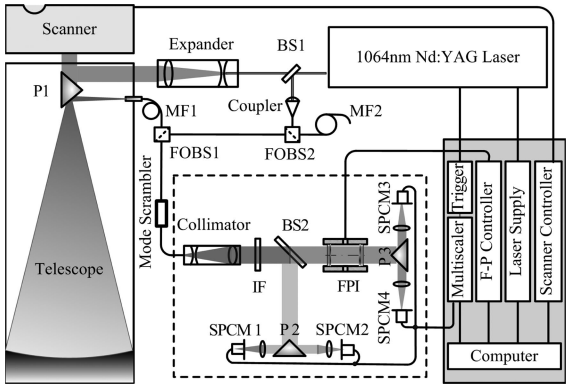

Fig. 2. Schematic of the lidar system: BS, beam splitter; P, prism; MF, multimode fiber; FOBS, fiber-optic beam splitter; IF, interference filter; SPCM, single photon counting mode; FPI, Fabry–Perot interferemeter.

is focused by a Cassegrain telescope into the Multimode Fiber (MF) 1, and then transferred into the receiver.

The receiver is shown in the dashed box in Fig. 2. After passing through an interference filter, the collimated light is split into two beams by BS2. The transmitted beam is sent through the FPI (IC Model ET50FS-1049), which uses a split structure with 30.2 nm cavity spacing difference between the two semicircle channels (as shown in Fig. 4). The signals that pass through the left channel and right one of the FPI are coupled onto two PerkinElmer single photon counting mode (SPCM) Si:APD detectors (where APD means avalanche photodide), respec-

Table 1. Parameters of the Doppler Lidar System

Instrument	Parameter
Transmitter	
Wavelength (nm)	1064
Laser energy (mJ/pulse)	200
Pulse width (ns)	6
Laser repetition rate (Hz)	50
Laser linewidth (MHz)	90
Transmitted beam divergence (mrad)	0.1
BS1 reflectance/transmittance	1/99
Receiver	
Telescope diameter (mm)	300
Telescope/scanner efficiency (%)	30
Telescope field of view (mrad)	0.15
BS2 reflectance/transmittance	1/3
Interference filter bandwidth (nm)	0.5
Interference filter efficiency (%)	40
SPCM quantum efficiency (%)	18
Fiber core diameter (μm)	100
Fiber numerical aperture	0.22
Fiber attenuation (dB/km)	1
Fabry–Perot interferometer	
Aperture (mm)	50
Cavity spacing (mm)	42.856
Step height (nm)	30.4
Plate reflectivity (%)	86.6
Acceptance angle (mrad)	1

tively. The reflected light from BS2 is also detected by two same monitoring detectors in case of asymmetry of the illumination on the FPI. The photon counting signals are binned in a multiscaler and integrated for a selectable number of shots prior to storage. The laser operation, FPI spacing/parallelism, and scanner orientation are controlled by an industrial computer. Software is developed to achieve real-time signal processing and unattended operation.

Some improvements had been made to the original DWL system [32]. A careful determination of the null Doppler-shift reference is necessary to get absolute winds measurements. In the original system, the position of the emitted wavelength in relation to the FPI bandpasses is determined by analyzing the light scattered off optics in the outgoing optic path. The deadtime correction of the SPCM can be different for the reference than for the atmospheric backscatter, since the laser pulse duration is only a few nanoseconds compared with the continuous atmospheric backscatter. This effect is difficult to compensate for, since the zero-wind reference spectrum can be affected independently of the Doppler-shifted spectra.

The problem was solved by using a second multimode fiber (MF2) when detecting the outgoing laser frequency (as shown in Fig. 2). Rayleigh scattering is related to the inhomogeneities due to the material structure. The optical fibers are well-known examples where the small refractive index fluctuations induced by their amorphous nature scatter light in all directions without changing the frequency of the scattered light, because the inhomogeneities are frozen in the material structure. The reference laser pulse was first focused into a 150 m long multimode fiber, and then the Rayleigh backscatter (RB) from MF2 was passed through the two fiber optical beam splitters (FOBS) and transferred into the receiver. The RB signal was used instead of the laser pulse to determine the reference frequency, since there is no frequency change between them. It is useful to step through the timing (see Fig. 3) for a single laser pulse to understand how the different signals are collected. The SYNC signal from the laser was used to synchronize the range-gating electronics. The signal collected in the ten bins before the Q switch was used to measure the averaging background. The RB signal from MF2 was collected in the five bins just after the Q switch. The output of the SPCM is disabled when a low level of transistor–transistor logic (TTL) is applied to its gate input. So the trigger to the SPCM could be used to eliminate the strong fiber-end reflections from MF2. The atmospheric backscatter was delayed by MF1 to avoid mixing with the RB from MF2. The final output data from the multiscaler is shown in Fig. 3.

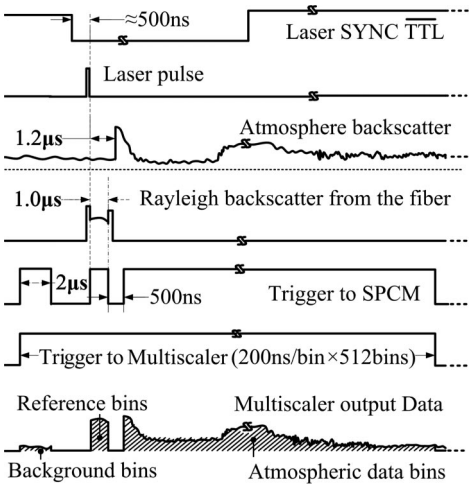

Fig. 3. Data acquisition timing sequence.

The MF1 is used as a time delayer to avoid mixture of the backscattered signals with the reference signals. It mixes the spatial intensity distribution of the energy collected from each range interval [25]. Range-dependent variations in the angular distribution of the collimated beam to the FPI cause its transmission function to vary with range [33]. To eliminate this effect on both the atmospheric backscatter and the reference signals incidence, a mode scrambler (Newport, FM-1) optimized for 100 μm core with graded-index fibers, is mounted on the transfer optical fiber. It presses the fiber between specially designed corrugated surfaces to cause microbending of the fiber and dramatically increases mode coupling among guided modes and coupling of high-order guided modes to radiation modes (mode filtering); thus, negligible insertion losses are introduced. The distribution of power among the modes is then independent of the launch condition of the light. The mode scrambler makes uniform the illumination onto the FPI, whether the original illumination pattern is a ring or a star. Two sets of typical experiments are shown in Fig. 4.

The long-term frequency drift of the outgoing laser with respect to the FPI has been controlled by a servo loop acting on the FPI tuning control. The laser frequency was located at the crossing point of the two transmission curves (as shown in Fig. 1). If the laser frequency deviates from that point, the transmission values on the dual channels for the RB signal from MF2 would be different. Then, a correcting voltage proportional to that differential signal would be fed back to the FPI piezoelectric drive. Therefore, the frequency of the outgoing laser could be locked at the crossing point with high sensitivity.

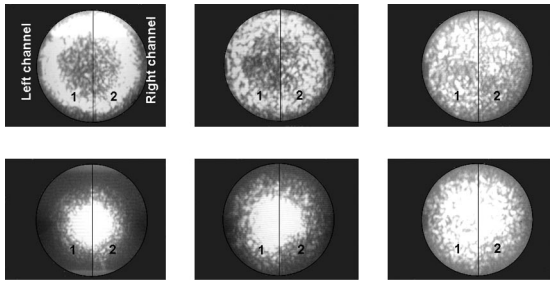

Fig. 4. Illumination patterns under the function of the mode scrambler.

4. Calibration

A. Instrument Calibration

DDL systems are usually less challenging than those required for optical heterodyning lidar. Much of this is due to the lack of need to accurately match wavefronts from the local oscillator and atmospheric echo on the heterodyne detectors. However, careful calibration procedures are required by the DDL systems. Using the RB from MF2, the ratio of the calibration constants a_1:a_2:a_3:a_4 can be measured by removing the FPI from the optical path and taking the ratio of the four SPCM detector signals.

To measure the FPI transmission curves, one can fix the cavity spacing and then scan the pressure, laser frequency, or angle of incidence. In this paper, the cavity scanning was performed with computer control using an IEEE-488 interface. The FPI is a piezoelectric-tunable and capacitive-servo-stabilized system. Its plates have a flatness of $\lambda/100$, where $\lambda = 632.8$ nm. The nonlinearity of the scan provided by the manufacturer is $\pm 0.05\%$. A capacitance bridge fabricated on the mirror plates is used to sense changes in parallelism and cavity spacing. Three piezoelectric actuators are used to turn the cavity spacing and permit elimination of parallelism errors. The FPI is designed to have a step height of 30.4 nm between the two semicircles on one mirror, so it is convenient for us to measure the two transmission curves simultaneously by scanning the cavity spacing through a spectral range about 2 GHz. The frequency scan range ν_s corresponding to the cavity scan range C_s depends on the FPI cavity spacing C_0:

$$\nu_s/C_s = \nu_0/C_0. \tag{20}$$

A plus or minus 10 mV differential voltage add to the piezoelectric drivers will stretch or shrink the piezoelectric tubes 1 nm, which equals 6.57 MHz frequency shift here. A 12 bit digital–analog (D/A) converter was used, so the argument writing to the IEEE-488 interface ranges from -2048 to 2047, corresponding to scan range from -1000 to 1000 nm.

The Si:APD detectors are capable of counting to 1.5×10^7 events per second before saturation; however, count rates are kept below 1.0×10^7 counts per second to ensure linearity. Moreover, the duration of the laser pulse is only 6.8 ns. If more than one photon is detected within this time, the detectors are at the risk of saturation. To have 600 photons detected on the edge detector at the peak transmission point, an integrating time of 12 s is needed for one scanning step. Usually, 200 sampling steps are used; then such a set of scanning is performed in less than 40 min. During such a long period, the laser frequency drifts and jitters would invalidate the measurement results. So, four Thorlab silicon p-i-n detectors were used to measure the transmission curves with both cw and pulsed laser in the earlier calibration procedure [29]. However, those results differ much from that measured with SPCM Si:APD detectors (as shown in Fig. 5); the peak transmission value

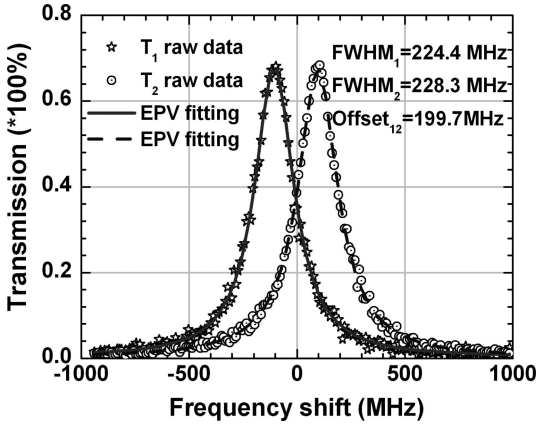

Fig. 5. FPI transmission curves for the pulsed laser.

changes more than 7%. Although all the detectors have the same fiber-optic receptacles prealigned to the anodes, the coupling efficiencies and the illuminations on the active area of the detectors may change when replacing the Si:APD detectors.

To keep simplicity and therefore reliability of the instrument, a fast FPI scanning method is proposed without replacing the detectors. This scanning method allows controlling of the FPI characteristics under the same conditions of illumination as during the wind detection. We replace MF2 (as shown in Fig. 1) by a 5000 m MF. The reference laser pulse was focused into it, and then the RB from the fiber was transferred into the receiver. It provides an atmospheric-backscatter-like continuous backscatter, which makes it possible to collect the signal in a time of 48 μs (corresponding to 240 bins on the multiscaler) for a single laser pulse. Approximately 3×10^4 photons can be detected on the edge detector on the peak transmission step with an integrating time of 2 s for each scanning step. The ensemble transmission curves can be scanned within 400 s after 3 h warmup of the laser, which allows for neglect of the frequency drift during the scanning process.

Given the calibration constants, transmission data $T(\nu_j)$ are calculated as a function of frequency by taking the ratio of the edge detector signals and the energy-monitoring detector signals (j is the scan index). Then we fit the results to an expanded pseudo-Voigt (EPV) function $f_{\mathrm{EVP}}(\nu)$ [34]. The formula of the EPV function was proposed by adding an irrational function and a squared hyperbolic secant function to the pseudo-Voigt function:

$$\begin{aligned} f_{\mathrm{EPV}}(\nu) = {} & (1 - \eta_L - \eta_I - \eta_P) f_G(\nu,\ w_G) + \eta_L f_L(\nu,\ w_L) \\ & + \eta_I f_I(\nu,\ w_I) + \eta_P f_P(\nu,\ w_P), \end{aligned} \tag{21}$$

where

$$f_G(\nu,\ \gamma_G) = \left(1/\pi^{1/2}\gamma_G\right)\exp\left(-\nu^2/{\gamma_G}^2\right) \tag{22}$$

is a Gaussian function with the FWHM given by $w_G = 2(\ln 2)^{1/2}\gamma_G$,

$$f_L(\nu,\ \gamma_L) = (1/\pi\gamma_L)(1 + \nu^2/\gamma_L{}^2)^{-1} \quad (23)$$

is a Lorentzian function with the FWHM of $w_L = 2\gamma_L$,

$$f_I(\nu,\ \gamma_I) = (1/2\gamma_I)[1 + (\nu/\gamma_I)^2]^{-3/2} \quad (24)$$

is an irrational function with the FWHM given by $w_I = (2^{2/3} - 1)^{1/2}\gamma_I$, and

$$f_P(\nu,\ \gamma_P) = (2/\gamma_P)[\exp(\nu/\gamma_P) + \exp(-\nu/\gamma_P)]^{-2} \quad (25)$$

is a squared hyperbolic secant function, of which the FWHM is given by $w_P = 2[\ln(2^{1/2} + 1)]\gamma_P$. Many factors, such as the divergence angle of the incidence beam, the aperture limitation, and the parallelism error of the plates, may distort the FPI transmission profiles from the Voigt function; thus, the EPV function is thought to be more flexible to proximate the actual FPI response functions for the pulsed laser. For the individual FPI channel, we let

$$T_{Mi}(\nu) = B + Af_{\mathrm{EVP}}(\nu - C), \quad (26)$$

where A is the integrated intensity, B is the constant background, and C is the center frequency. Numerical least-squares optimization of the EPV function is achieved by the Levenberg–Marquardt method, applying the weight $T^{-1/2}(\nu_j)$. Then the function to be minimized is

$$S = \sum_{j=1}^{200} [T(\nu_j) - (B + Af_{\mathrm{EVP}}(\nu_j - C))]^2/T(\nu_j). \quad (27)$$

All parameters, A, B, C, and width parameters, w_G, w_L, w_I, w_P and mixing parameters, η_L, η_I, η_P, in Eq. (27), are treated as independent variables.

It has been claimed that the maximum deviation of EPV function from the Voigt function is within 0.12%, which can be tolerated in this context [34]. A typical example of the scanning experiments is shown in Fig. 5. The standard deviation of the raw data from the fitted EPV function on channel 1 is 0.76%, and 0.83% on the other channel for frequency shift $|\Delta\nu| <$ 100 MHz. In the lidar initializing processes, to set the FPI symmetrically to the laser frequency, the voltages added to the piezoelectric actuators are different from time to time. However, a good repeatability of the transmission curves is kept. The transmission curves were scanned every day for 20 days, the standard deviation of peak value is 0.49%, and the standard deviation of the FWHM is 0.36%.

B. Verifying Attachment

A verifying attachment was designed to validate the calibration constants and the FPI transmission functions for the laser pulse. The basic principle is to make a comparison between experimental results measured by the DWL system and the known velocities of the revolving disk. Detailed design of the verifying attachment was given elsewhere [35]. Figure 6 is the schematic of the verifying attachment. The cross-talk signal from the fused fiber coupler (FFC) 1 was used as the reference signal to decide the frequency of the outgoing laser. A 300 m MF that connects FFC1 and the fiber pigtailed collimator was used as a time delayer. Using the pulsed laser and the range-gated analyzer permits the outgoing laser pulse and the backscatter from the rim of the disk to be separated temporally. Therefore, the reference signal and the Doppler-shifted signal scattered from the revolving disk were collected in different bins. Since all fiber-optic components are used, the verifying attachment is portable with volume of 346 mm $\times$ 285 mm $\times$ 175 mm and weight of 14 kg. The designed relative error of the verifying attachment is less than 1% within the dynamic range of $\pm$50 m/s. The maximum spectrum broadening corresponding to the designed Teflon disk has a width of 0.7 MHz, which is similar to the aerosol circumstance.

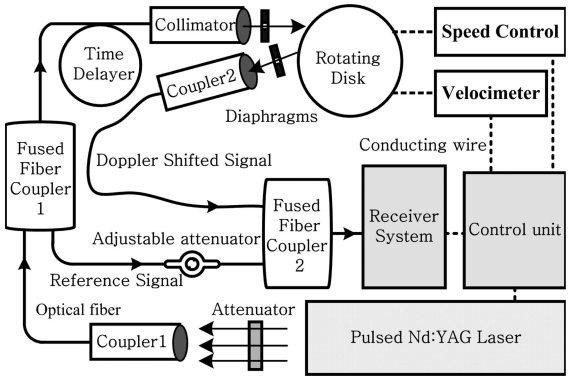

Fig. 6. Schematic of the verifying attachment.

Figure 7 shows the velocities measured by lidar versus preset velocities on the verifying attachment. Each data point is an averaging result of 100 measurements. By improving the signal intensity or using longer integration time, more accurate experiment data may result. Here, for each experiment, an integration time of 1 min was used; and more than 4000 photons were counted on each energy monitoring detectors. The

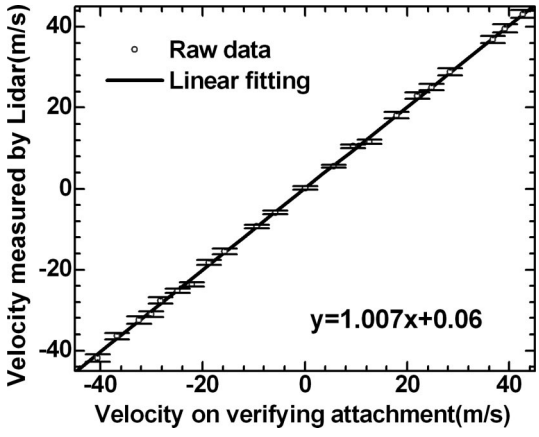

Fig. 7. Calibration: comparison between two results.

slope of linear fitting, in a least-squares sense, is 1.01. The value is slightly higher than an idealized slope of unity. This may be due to the expansion of the Teflon disk at a high rotating speed. The standard deviation of the measurements is 0.63 m/s for target velocity $|v| < 20$ m/s, whereas the value is 0.96 m/s for target velocity $|v| < 45$ m/s.

C. Error Analysis

We consider measurement error in the previously described experiment in Section 4. If the laser frequency ν_0 is set at the center of symmetry of the two channels, the transmissions of the two channels for the backscatter signal from a hard target will be identical at zero-Doppler shift. The transmission difference between the two passbands provides the Doppler-shift information. Expanding the transmission difference in a power series, the zero-order terms cancel, and the first-order terms are adequate for determining the accuracy of measurement of small Doppler shifts:

$$T_{M2}(\nu_1) - T_{M1}(\nu_1) = \Delta\nu_d\left(\frac{\mathrm{d}T_{M2}}{\mathrm{d}\nu} - \frac{\mathrm{d}T_{M1}}{\mathrm{d}\nu}\right)_{\nu_0}, \quad (28)$$

where $\nu_1 = \nu_0 + \Delta\nu_d$ is the Doppler-shifted frequency. Then, the uncertainty in the Doppler-shift measurement is

$$\delta(\Delta\nu_d) = \delta[T_{M2}(\nu_1) - T_{M1}(\nu_1)] \Big/ \left(\frac{\mathrm{d}T_{M2}}{\mathrm{d}\nu} - \frac{\mathrm{d}T_{M1}}{\mathrm{d}\nu}\right)_{\nu_0}. \quad (29)$$

In the experiments discussed in Section 4, the incident signal is the backscattering from the hard target. The transmissions $T_{M2}(\nu_1) = a_4 I_2 / a_2 I_{E2}$ and $T_{M1}(\nu_1) = a_3 I_1 / a_1 I_{E1}$ are calculated using the signals on the four detectors. We let $\Delta T_M = T_{M2}(\nu_1) - T_{M1}(\nu_1)$. The photon noise of both edge and energy monitor channels are uncorrelated and follow Possion statistics with signal-to-noise ratio inversely proportional to the square root of signal counts on each detector. Then,

$$\delta^2(\Delta T_M) = \sum_{j=1}^{2}\left[\left(\frac{\partial \Delta T_M}{\partial I_j}\right)^2 (\delta I_j)^2 + \left(\frac{\partial \Delta T_M}{\partial I_{Ej}}\right)^2 (\delta I_{Ej})^2\right], \quad (30)$$

where the uncertainties δI_j and δI_{Ej} are approximately given by the square root of all photon counts (including backscatter signal, background signal, detector noise, etc.) on corresponding detectors. Use of Eq. (30) in Eq. (29) yields the uncertainty in the Doppler shift measurement:

$$\delta_1(\Delta\nu_d) = \left[\left(\frac{a_4}{a_2}\right)^2\left(\frac{I_2^2}{I_{E2}^3} + \frac{I_2}{I_{E2}^2}\right) + \left(\frac{a_3}{a_1}\right)^2\left(\frac{I_1^2}{I_{E1}^3} + \frac{I_1}{I_{E1}^2}\right)\right]^{1/2} \Big/ \left(\frac{\mathrm{d}T_{M2}}{\mathrm{d}\nu} - \frac{\mathrm{d}T_{M1}}{\mathrm{d}\nu}\right)_{\nu_0}. \quad (31)$$

Equation (31) gives the error only for shot noise of the backscattered signal. Errors in determination of the outgoing laser frequency must also be considered, and this frequency is ideally determined using the same frequency discriminator. Generally, the reference error δ_R is small, because adequate reference signals are available by taking advantage of the continuous RB signal from the MF as described in Section 3. Nonetheless, the complete error δ_C has to incorporate the reference error:

$$\delta_C = \left(\delta_1^2(\Delta\nu_d) + \delta_R^2\right)^{1/2}. \quad (32)$$

Various systematic errors contributed to the total error in Fig. 7. A significant component of the measured standard deviation was introduced by the vibration of the hard target at high speed. To reduce this error and to make a comparison between theoretical analysis and the experiment results, the verifying attachment was set to a low LOS velocity of 5 ms^{-1} (corresponding sensitivity of the lidar is 4.3%/ms^{-1}). By modulating the signal intensity and varying the integration time, nine sets of 100 data measurements were conducted.

Given the photon counts in all channels, one can calculate the theoretical standard deviations according to Eq. (32) and the Cramer–Rao lower bound. The statistical noise measurement limit, based on sampling theory, has been described by Rye [36] and applied to the aerosol backscatter wind lidar based on the double-edge technique by McKay [15]:

$$\delta_2(\Delta\nu_d) = \frac{\left(1 + 4\gamma_0^2\right)^{3/2}}{8\gamma_0}\left(\frac{1}{2\rho T_{pk} N_0 \eta}\right)^{1/2} w, \quad (33)$$

where, in this paper, $\gamma_0 \approx 0.5$ is the operating point of the FPI, $\rho \approx 0.37$ is the proportion of incident signal delivered to each FPI channel, η is the SPCM quantum efficiency, $w \approx 226$ MHz is the passband FWHM of the FPI, $T_{pk} \approx 0.68$ is the peak transmittance (as shown in Fig. 5), and N_0 is the total incident photon number.

The measured standard deviations and the expressions (31) and (33) are compared. It can be seen from Fig. 8 that with the parameters we described, the theoretical standard deviations proposed in this paper and McKay's estimation are nearly the same. The measured standard deviations for each preset signal intensity and integration time are slightly higher than the theoretical standard deviations, with an average difference of 20 cm s^{-1}. A standard deviation of 5 cm s^{-1} is introduced by the uncertainty of the target speed. The errors due to uncertainties in the system parameters and spectral calibrations are estimated from the 15 day standard deviations to be 11 cm s^{-1}. Although the double-edge technique renders the measurement insensitive to laser and filter frequency jitter and drift, a residual error of 1 cm s^{-1} is contributed to the speed measurement. Additional possible error sources included errors that are due to residual

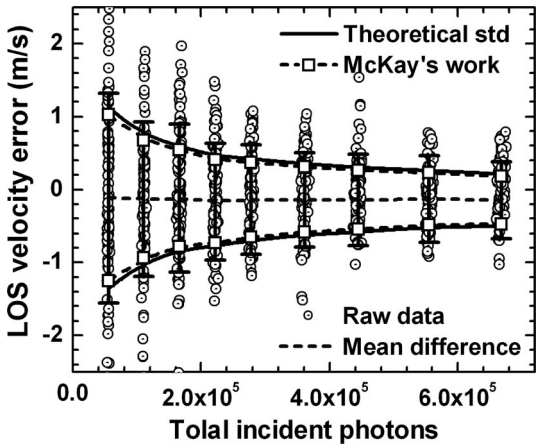

Fig. 8. Velocity accuracy versus total incident photons at LOS speed of 5 m/s. The raw data are shown as circles, and the experimental standard deviations are shown as error bars. The theoretical standard deviations described in this paper are shown as solid curves. The statistical noise measurement limit proposed by McKay [15] are shown as dashed curves with squares.

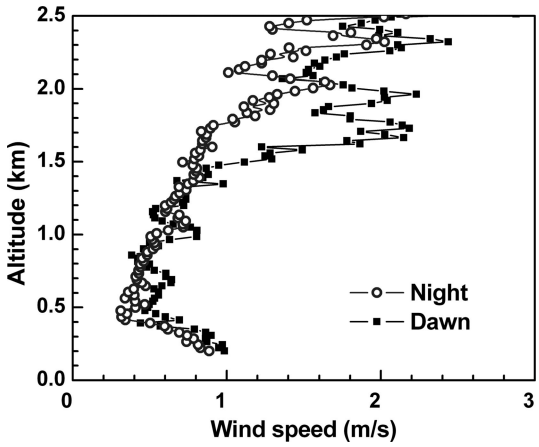

Fig. 10. Standard deviation of the LOS wind as a function of altitude for 50-shot averages with a sample of 1000 shots. The measured data at night are shown as circles and the daytime data are shown as filled squares.

nonlinearities and the dark count of the single photon-counting modules. The mean difference between lidar observations and the preset velocity is 9 cm s^{-1}.

The verifying experiments and the comparison between theoretical analysis and measured standard deviations well validated the instrument calibration results. Considering other intrinsic errors, the theoretical analysis well estimates the measured standard deviations. In field measurements, the Rayleigh components in the atmospheric backscattering and the background noise must be considered. This has been discussed by both McKay [15] and McGill and Spinhirne [17].

5. Lidar Wind Measurements

A. Comparison Experiments

The ground-based DWL is located on the flight course of Hefei city. Rawinsonde data are unavailable to validate the lidar performance in that area. Recently, we had an opportunity to make comparison experiments between the DWL and another newly built wind profiler radar (WPR, 450 MHz) located ~450 m from the lidar.

Experiments were carried out from 15–30 July 2006. The spatial resolution of the WPR is ~100 m over the altitude and its temporal resolution is 30 min. The wind speed errors and direction errors of the WPR are expected to be less than 1 m/s and 10°, respectively.

Two typical experiment results are shown in Fig. 9. Mean wind speed and direction measured from DWL are shown with $\pm\sigma$ error bars calculated for the three profiles measured during the 30 min. The standard deviation averaged over altitude is 0.45 m/s with a maximum value of 2.7 m/s from 1:30 to 2:00 a.m., and it is 0.61 m/s with a maximum value of 2.4 m/s from 6:30 to 7:00 a.m.

The data of Fig. 9 were analyzed to distinguish the instrumental error from geophysical variability. We calculated the standard deviation of the LOS wind as a function of altitude for 50-shot averages with a sample of 1000 shots, i.e., the standard deviation of 20 wind measurements at each altitude (as shown in Fig. 10). The standard deviation below 1500 m is

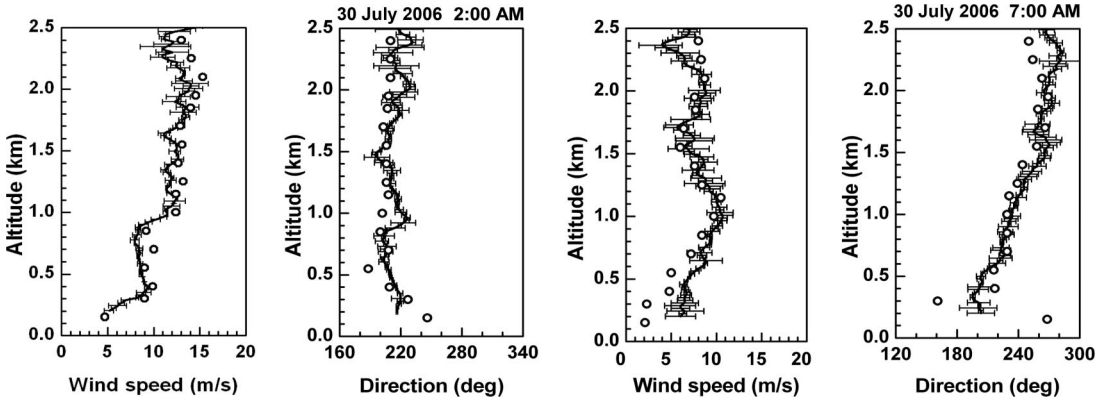

Fig. 9. Horizontal wind and direction profiles measured by Doppler wind lidar (solid curve) and wind profiler radar (circle).

lower than 1 m s^{-1} at dawn and night. The standard deviation below 500 m is larger than the value from 500 to 1000 m. This was mainly attributed to range-dependent variations in both the angular distribution of the collimated beam to the FPI and the nonlinearity of the detectors.

The wind and direction data from the DWL and WPR show good consistency in Fig. 9, but there are some differences between the two results. The time interval for photon-counting accumulation for radial wind is 1 min and the vertical sampling is 21.2 m for DWL, so the difference of direction at 2:00 a.m. at the altitude of 1 km could be due to wind shear. The horizontal wind velocity measured by WPR deviated from the profile probed by DWL at 7:00 a.m. in the low altitude; this could be due to the WPR system being affected by the echoes from its surroundings. From Fig. 10, we know that the standard deviation in Fig. 9 increased rapidly in the altitude below 400 m at dawn due to the inhomogeneity of the wind field.

Another experiment was made with Vaisala wiresonde to evaluate the accuracy of DWL quantitatively. The lidar system was built on the roof of the main building, and its altitude is 36.6 m. In the experiment, the laser beam was sent out in the direction of the wiresonde horizontally. The temporal resolution of DWL was set to 1 min, while there were several measurement results from the wiresonde during the interval. So, the wiresonde data were averaged every minute and transformed into LOS horizontal speed along the DWL azimuth for the purpose of comparison. The wind speed errors and direction errors of the wiresonde are expected to be 0.5 m/s and 10°, respectively. The wiresonde should be recharged every 2 h. It was hung on the pilot balloon at an altitude of 40 m, just beyond the laser beam. The horizontal distance between the lidar and the wiresonde is 480 m. Experiments were conducted from 14–18 September 2006. Two typical experimental results are shown in Fig. 11. The spike points in the wiresonde data may be due to its wobble in the wind. The stronger the wind, the more spikes were detected. These invalid data were removed in the comparison process.

The histogram presented in Fig. 12 summarizes the differences between the DWL and wiresonde LOS winds for the 5 days. The mean difference is 5 cm/s. This bias may be due to uncertainties in the system parameters and spectral calibrations during the 5 days (as described in Subsection 4.A). The differences in Fig. 12 are narrowly and normally distributed with a standard deviation of 1.15 m/s. This is in good agreement with the standard deviation in Fig. 9, considering that an additional standard deviation of 0.5 m/s was contributed to the wobble of the wiresonde.

B. Lidar Observations

Following the testing and calibration experiment, we started making continuous wind field observation in November 2005. Continuous operation of the lidar

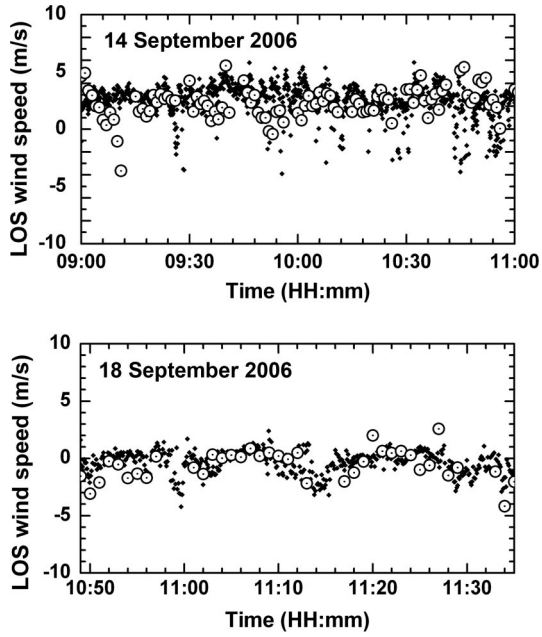

Fig. 11. LOS wind measured with DWL and wiresonde. The wind lidar measurements are shown as circles and the wiresonde data are shown as filled squares.

can produce a time series of wind profile data to capture dynamics within the boundary layer. A 24 h observation conduct on 27 April 2006 is shown in Fig. 13. The elevation angle was 45°, the range resolution is 30 m, and the temporal resolution is 10 min per wind profile. The data are integrated over 1 min for each fixed elevation angle along each of the three cardinal directions. In the wind observation, the Rayleigh and aerosol components of the atmospheric backscatter are separated. We assume that errors in measured component velocities are dominated by the shot noise in the detected signals. The three direction radial wind profiles are combined to derive the wind speed and direction. In this process, the wind measurement errors are evaluated. The tolerated wind speed error is 3 m s^{-1}, i.e., the measured results with error greater than 3 m s^{-1} are not plotted. Figures

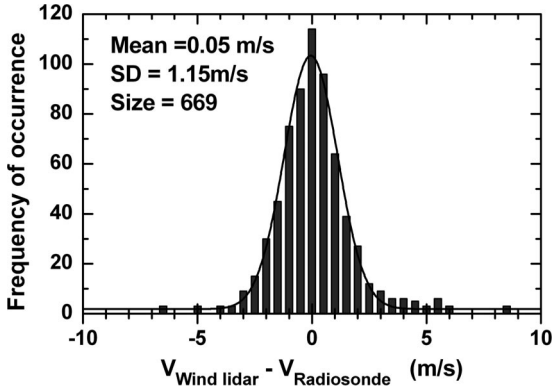

Fig. 12. Histogram of differences between corresponding pairs of 1 min LOS projected horizontal wind velocities for the wiresonde and DWL.

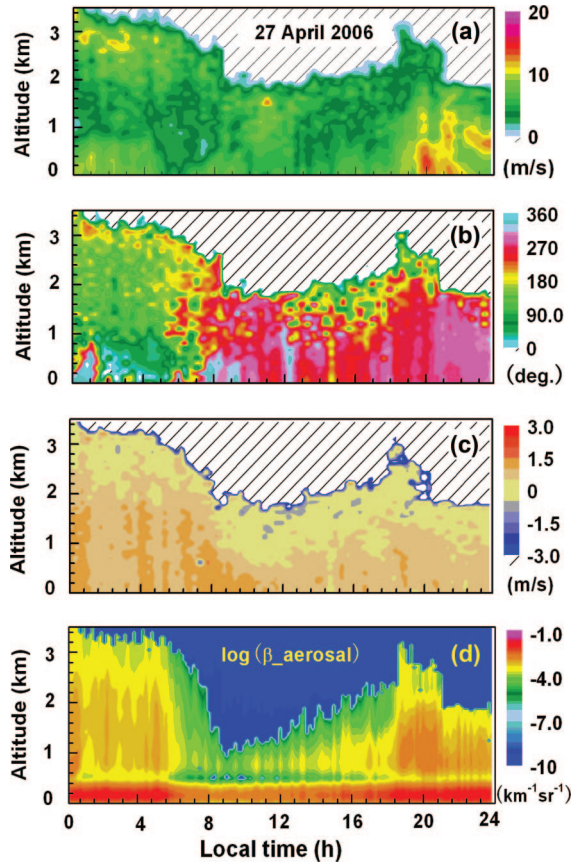

Fig. 13. 24 h observation of wind field and aerosol backscatter coefficient on 27 April 2006: (a) time-height plot of horizontal wind velocity, (b) wind direction, (c) vertical wind velocity, (d) time–height plot of aerosol backscatter coefficients in logarithmic scale.

13(a) and 13(b) are the time-height plot of horizontal wind components and wind directions, respectively. The wind direction became unsteady at sunrise. Of particular interest is the notable wind speed drop and wind direction change observed at 7:20 a.m. After sunset, wind speed increased from 9 to 17 ms^{-1} in the lowest altitude from 7:30 to 8:00 p.m., which is coincident with the wind speed measured by the anemometer outside our laboratory. Figure 13(c) shows the vertical components of wind. The red contours indicate downward motion and blue contours indicate upward motion. Much of the time the contours were light blue and light red, which, indicates that particles were falling or rising at approximately 0–2 m/s. Considering the lidar observation is based on aerosol backscatter, we retrieved the aerosol backscatter coefficients simultaneously [29–31]. Figure 13(d) is the time-height plot of aerosol backscatter coefficients during the 24 h. It is obvious that as altitude increases, the aerosol backscatter coefficients decrease, and both the horizontal wind speed error and vertical wind speed error increase accordingly.

6. Conclusion

Several important improvements were performed to our original lidar system. Using Rayleigh signal backscattered from a multimode optical fiber as the reference signal provides us more accurate measurements in both the calibration process and the outgoing laser frequency determination. A more flexible expanded pseudo-Voigt function was used to proximate the actual response function for the pulsed laser. A mode scrambler mounted on the transfer fiber substantially improves the uniformity of the illumination to the FPI. The stability of FPI transmission curves as maintained with a standard deviation of peak value of 0.49% within 20 days. The calibration results were validated by using a verifying attachment. We also performed a comparison between theoretical analysis and measured errors. Considering some intrinsic instrumental errors, the theoretical analysis can well estimate the actual measured errors. Comparisons with WPR show good coincidence and the lidar's ability to detect wind shear in troposphere. Further comparisons with the Vaisala wiresonde also show good agreement, and the standard deviation is coincident with the WPR comparison results. Continuous operation of the lidar provides horizontal and vertical information of the wind field and the aerosol backscatter coefficients. Atmospheric dynamics were observed in the continuous operation.

The authors acknowledge the contributions of Ningquan Wen and Jun Zhou, who provided wind profiler radar data and Vaisala wiresonde data in the comparisons.

References

1. World Meteorological Organization, "Preliminary statement of guidance regarding how well satellite capabilities meet WMO user requirements in several application areas," WMO Satellite Reports SAT-21, WMO/TD 913 (1998).
2. W. E. Baker, G. D. Emmitt, F. Robertson, R. M. Atlas, J. E. Molinari, D. A. Bowdle, J. R Paegle, R. M. Hardesty, R. T. Menzies, T. N. Krishnamurti, R. A. Brown, M. J. Post, J. R. Anderson, A. C. Lorenc, and J. McElroy, "Lidar-measured winds from space: a key component for weather and climate prediction," Bull. Am. Meteorol. Soc. **76,** 869–888 (1995).
3. F. F. Hall, R. M. Huffaker, R. M. Hardesty, M. Jackson, T. R. Lawrence, M. Post, R. A. Richter, and B. F. Weber, "Wind measurement accuracy of the NOAA pulsed infrared Doppler," Appl. Opt. **23,** 2503–2506 (1987).
4. R. M. Huffaker and R. M. Hardesty, "Remote sensing of atmospheric wind velocities using solid-state and CO_2 coherent laser systems," Proc. IEEE **84,** 181–204 (1996).
5. M. L. Chanin, A. Garnier, A. Hauchecorne, and J. Porteneuve, "A Doppler lidar for measuring winds in the middle atmosphere," Geophys. Res. Lett. **16,** 1273–1276 (1989).
6. A. Garnier and M. L. Chanin, "Description of a Doppler Rayleigh lidar for measuring winds in the middle atmosphere," Appl. Phys. B **55,** 35–40 (1992).
7. C. L. Korb, B. M. Gentry, S. X. Li, and C. Flesia, "Theory of the double-edge technique for Doppler lidar wind measurement," Appl. Opt. **37,** 3097–3104 (1998).
8. C. Flesia and C. L. Korb, "Theory of the double-edge molecular technique for Doppler lidar wind measurement," Appl. Opt. **38,** 432–440 (1999).
9. J. Wu, J. Wang, and P. B. Hays, "Performance of a circle-to-line optical system for a Fabry–Perot interferometer: a laboratory study," Appl. Opt. **33,** 7823–7828 (1994).

10. T. D. Irgang, P. B. Hays, and W. R. Skinner, "Two-channel direct-detection Doppler lidar employing a charge-coupled device as a detector," Appl. Opt. **41,** 1145–1155 (2002).
11. C. Nagasawa, Y. Shibata, M. Abo, T. Nagai, and O. Uchino, "Incoherent Doppler lidar using wavelengths for wind measurement," in *Lidar Remote Sensing for Industry and Environment Monitoring,* U. Singh, T. Itabe, and N. Sugimoto, eds., Proc. SPIE **4153,** 338–349 (2001).
12. Z.–S. Liu, D. Wu, J.–T. Liu, K.–L. Zhang, W.–B. Chen, X.–Q. Song, J. W. Hair, and C. Y. She, "Low-altitude atmospheric wind measurement from the combined Mie and Rayleigh backscattering by Doppler lidar with an iodine filter," Appl. Opt. **41,** 7079–7086 (2002).
13. J. A. McKay, "Assessment of a multibeam Fizeau wedge interferometer for Doppler wind lidar," Appl. Opt. **41,** 1760–1767 (2002).
14. D. Bruneau, A. Garnier, A. Hertzog, and J. Porteneuve, "Wind-velocity lidar measurements by use of a Mach–Zehnder interferometer, comparison with a Fabry–Perot interferometer," Appl. Opt. **43,** 173–182 (2004).
15. J. A. McKay, "Modeling of direct-detection Doppler wind lidar. I. The edge technique," Appl. Opt. **37,** 6480–6486 (1998).
16. J. A. McKay, "Modeling of direct-detection Doppler wind lidar. II. The fringe imaging technique," Appl. Opt. **37,** 6487–6493 (1998).
17. M. J. McGill and J. D. Spinhirne, "Comparison of two direct-detection Doppler lidar techniques," Opt. Eng. **37,** 2675–2686 (1998).
18. Y. Durand, A. Culoma, R. Meynart, D. Morançais, and F. Fabre, "Predevelopment of a direct-detection Doppler wind lidar for ADM/AEOLUS mission," in *Sensors, Systems, and Next-Generation Satellites VII,* R. Meynart, S. P. Neeck, H. Shimoda, J. B. Lurie, and M. L. Aten, eds., Proc. SPIE **5234,** 354–363 (2004).
19. C. Souprayen, A. Garnier, A. Hertzog, A. Hauchecorne, and J. Porteneuve, "Rayleigh–Mie Doppler wind lidar for atmospheric measurements. I. Instrumental setup, validation, and first climatological results," Appl. Opt. **38,** 2410–2421 (1999).
20. C. Souprayen, A. Garnier, and A. Hertzog, "Rayleigh–Mie Doppler wind lidar for atmospheric measurements. II. Mie scattering effect, theory, and calibration," Appl. Opt. **38,** 2422–2431 (1999).
21. C. Flesia, C. L. Korb, and C. Hirt, "Double-edge molecular measurement of lidar wind profiles at 355 nm," Opt. Lett. **25,** 1466–1468 (2000).
22. B. M. Gentry, H. Chen, and S. X. Li, "Wind measurements with 355 nm molecular Doppler lidar," Opt. Lett. **25,** 1231–1233 (2000).
23. V. J. Abreu, J. E. Barnes, and P. B. Hays, "Observations of winds with an incoherent lidar detector," Appl. Opt. **31,** 4509–4514 (1992).
24. K. F. Fischer, V. J. Abreu, W. R. Skinner, J. E. Barnes, M. J. McGill, and T. D. Irgang, "Visible wavelength Doppler lidar for measurement of wind and aerosol profiles during day and night," Opt. Eng. **34,** 499–511 (1995).
25. C. L. Korb, B. M. Gentry, and S. X. Li, "Edge technique Doppler lidar wind measurements with high vertical resolution," Appl. Opt. **36,** 5976–5983 (1997).
26. M. J. McGill, W. R. Skinner, and T. D. Irgang, "Validation of wind profiles measured with incoherent Doppler lidar," Appl. Opt. **36,** 1928–1938 (1997).
27. M. Imaki and T. Kobayashi, "Ultraviolet high-spectral-resolution Doppler lidar for measuring wind field and aerosol optical properties," Appl. Opt. **44,** 6023–6030 (2005).
28. G. Tenti, C. D. Boley, and R. D. Desai, "On the kinetic model description of Rayleigh–Brillouin scattering from molecular gases," Can. J. Phys. **52,** 285–290 (1974).
29. J. D. Klett, "Stable analytical inversion solution for processing lidar returns," Appl. Opt. **20,** 211–220 (1981).
30. J. D. Klett, "Lidar inversion with variable backscatter extinction ratios," Appl. Opt. **24,** 1638–1643 (1985).
31. F. G. Fernald, "Analysis of atmospheric lidar observations: some comments," Appl. Opt. **23,** 652–653 (1984).
32. D. Sun, Z. Zhong, J. Zhou, H. Hu, and T. Kobayashi, "Accuracy analysis of the Fabry–Perot based Doppler wind lidar," Opt. Rev. **12,** 409–414 (2005).
33. C. J. Grand and E. Eloranta, "Fiber-optic scrambler reduces the bandpass range dependence of Fabry–Perot etalons used for spectral analysis of lidar backscatter," Appl. Opt. **30,** 2668–2670 (1991).
34. T. Ida, M. Ando, and H. Toraya, "Extended pseudo-Voigt function for approximating the Voigt profile," J. Appl. Crystallogr. **33,** 1311–1316 (2000).
35. H. Xia, D. Sun, Z. Zhong, B. Wang, J. Dong, F. Shen, M. Chen, and X. Zhou, "A design of verifying attachment for calibration of wind lidar," Chin. J. Lasers **33,** 1412–1416 (2006) (in Chinese).
36. B. J. Rye, "Comparative precision of distributed-backscatter Doppler lidars," Appl. Opt. **34,** 8341–8344 (1995).